Efficient isogeometric boundary element method for analysis of acoustic scattering from rigid bodies

A. M. A. Alsnayyan, J. Li, S. Hughey, A. Diaz, and B. Shanker

Citation: The Journal of the Acoustical Society of America **147**, 3275 (2020); doi: 10.1121/10.0001182
View online: https://doi.org/10.1121/10.0001182
View Table of Contents: https://asa.scitation.org/toc/jas/147/5
Published by the Acoustical Society of America

JASA ARTICLE

Efficient isogeometric boundary element method for analysis of acoustic scattering from rigid bodies

A. M. A. Alsnayyan,[1,a)] J. Li,[1] S. Hughey,[1] A. Diaz,[2] and B. Shanker[1]
[1]*Department of Electrical and Computer Engineering, Michigan State University, Lansing, Michigan 48824, USA*
[2]*Department of Mechanical Engineering, Michigan State University, Lansing, Michigan 48824, USA*

ABSTRACT:
Boundary integral analysis of scattering from rigid bodies is well known. Analysis often proceeds along the following lines: representation of the geometry using a collection of triangles, representation of physics using low order ansatz functions defined on each triangle, and then solving the resulting discrete system. This prescription for the common solution stands out in terms of the low-order approximation of both geometry and representation of physics; specifically, both are C^0. Taking inspiration from computer graphics literature, a framework wherein continuity of representation (both geometry and physics) can be as high as C^2 is developed. In this paper, the steps necessary to develop such a iso-geometric (i.e., using the same basis functions for representing both geometry and physics) boundary integral solver are elucidated. In doing so, an efficient method based on a wideband fast multipole method to evaluate the required inner products and matrix vector products is proposed and demonstrated. Numerous examples are presented to highlight the benefits of the proposed approach. © *2020 Acoustical Society of America*.
https://doi.org/10.1121/10.0001182

(Received 22 October 2019; revised 9 April 2020; accepted 14 April 2020; published online 7 May 2020)
[Editor: Nail A. Gumerov] Pages: 3275–3284

I. INTRODUCTION

Surface integral equation (SIE) methods for computing fields scattered from piecewise homogeneous scatterers have been well studied and understood,[1–3] so much so that they are now commonplace. As is well known, SIE formulations present several benefits: (a) the Green's function embeds the necessary radiation condition; (b) reduction of a volumetric problem into a surface embedded in a volume, and therefore, the required degrees of freedom; and (c) readily handle arbitrary geometries. Traditional downsides of these methods are (a) non-uniqueness at irregular frequencies[4] and (b) computational complexity that scales as $\mathcal{O}(N_b^2)$, where N_b denotes the number of degrees of freedom used in the analysis.[5] By computational complexity, we refer to the scaling of memory required as well as execution time of each matrix vector product required in any iterative solver. We note that both downsides have been overcome.[6] Methods have been developed to obtain a unique solution at all frequencies and to reduce the cost to $\mathcal{O}(N_b \log N_b)$.[7,8] Given these advances, SIE-based computational methods are both reliable and robust.

However, despite all appearances, a number of interesting challenges remain and these are not specific to acoustics. Indeed, as will be evident in this paragraph, some of these comments apply to all SIEs. A traditional SIE solution proceeds as follows: The surface of a candidate object is represented using a collection of discrete elements, the physical quantity of interest is then represented using basis functions described on these discrete elements, and a variational technique is used to reduce the continuous equations to a set of discrete equations. Typically, the object is represented using a collection of triangles, and low order ansatz basis functions are used to represent the physical quantity of interest on the scatterer. The resulting discrete set inherits (and depending on the operator, exacerbates) errors due to geometric approximation. It follows, then, that these challenges can be alleviated by resorting to higher order geometric representation and the corresponding basis functions.[9] One would imagine that resorting to higher order geometric representation would result in fewer degrees of freedom, simply due to the fact that one does not need as many piece-wise flat triangles to represent the object. But one should note that in most higher order schemes, the discretization is still C^0 and functions are higher order within *one* triangle. Our approach to higher order analysis is different.

In the past, we developed a method for discretizing SIEs that was highly flexible and adaptive called the generalized method of moments (GMM).[10,11] GMM is effective and efficient, and has been used for different problems in both acoustics and electromagnetics. It permits refinement in the order of geometric representation and the order of basis functions used for physics, and spatial refinement. In GMM, geometry is constructed using a set of overlapping patches, with physical basis functions defined on each patch. Since each patch is constructed using a least-squares approach, a persistent drawback of GMM is that these parametrizations are *not* watertight.

Robust higher order watertight surface representation is indeed vogue in the computer graphics literature. Here, the

a)Electronic mail: alsnayy1@msu.edu

surface representation is watertight and approximately C^2 almost everywhere (provided one uses subdivision[12,13]). The higher order continuity of the surface representation offers a number of tantalizing opportunities from both mathematical and engineering perspectives such as analysis of convergence, development of Calderón type preconditioners, Laplace-Beltrami based compression, higher order basis for physics that has the same continuity properties as geometric basis sets, shape, and topology optimization methods that rely on compressed systems, and so on. In this paper, we set the stage for this body of work by asking a more fundamental question—what should we have in our arsenal so as to realize computationally efficient higher order (in geometry and physics) analysis tools.

Our approach to meeting the goals alluded to earlier is to use isogeometric analysis. Here, the basis functions used to represent the physics are the *same* as basis functions used to represent the geometry. As a result, all the geometric modeling features that one desires, such as adaptivity, refinement, etc., directly carry over to modeling the physics. In a manner of speaking, in the long term such an analysis tool would enable seamless integration of computer aided design (CAD) and computer aided engineering (CAE). The advent of isogeometric analysis has its genesis in early papers by Hughes,[14] and has since been adapted for a number of different types of problems[15,16] in structural mechanics and electromagnetics.[17–19]

While our earlier body of work on extending isogeometric analysis based on subdivision surfaces to electromagnetics[17,18,20] demonstrated its viability, several challenges related to computational cost, both evaluation of matrix elements as well as matrix vector products, were left unaddressed. It is important to note that the Green's kernels used for electromagnetics were all due to single layer potentials, unlike those for acoustics.[21] The latter makes evaluation significantly more challenging. To help visualize challenges in evaluating the necessary inner products, it should be noted that unlike Lagrangian discretization, the domain of a subdivision basis function is significantly larger; it includes all triangles that share a node (or control point). The basis function used for geometry is a product of box-splines and therefore, fourth order. Since we use the same basis function for physics as well, it implies that one needs to evaluate products of higher order polynomials convolved with a Green's function on higher order surfaces, for all pairwise interactions as is dictated by an SIE formulation. Assuming that N_b is the number of degrees of freedom, and N_q is the number of quadrature points, the cost of evaluating the matrix elements scales as $\mathcal{O}(N_q^2 N_b^2)$. We note that N_q can be very high as both the surface and the basis functions are fourth order polynomials. Our *twin objectives* in this paper are to (a) develop an isogeometric analysis technique for acoustic scattering that is (b) computationally efficient. Specifically, we seek to reduce the cost of evaluation of both the matrix elements as well as a matrix vector product. To effect this reduction, we exploit a version of the multi-level fast multipole method (MLFMA) that is stable at both low and high frequencies[22,23] and has been used extensively for wideband electromagnetic analysis. To this end, the principal contributions of this paper are as follows: We present

- isogeometric analysis (IGA) on smoothly represented structures of arbitrary topology,
- a study of convergence properties of IGA based SIE solvers,
- methods to linearize both the cost of evaluation of the necessary matrices and matrix-vector products,
- a demonstration of convergence of IGA-SIE solver for conical geometries as well as complex targets with multiscale features, and
- results validating the scaling and accuracy of wideband MLFMA scheme.

The rest of the paper is organized as follows; in Sec. II, we present the formulation, describe subdivision basis for geometry, and discuss the resulting linear system. In Sec. III, we present a methodology to efficiently evaluate all the requisite inner products. This is followed by asymptotic complexity estimates in Sec. IV, and a slew of numerical results in Sec. V. Finally, in Sec. VI, we summarize our contributions.

II. FORMULATION AND ANALYSIS FRAMEWORK

In what follows, we formally pose the problem under consideration, present a subdivision representation of the geometry, prescribe basis sets and derive a discrete matrix system that needs to be solved.

A. Problem statement

Consider a scatter, in a homogeneous medium, with a hard boundary $\Omega \in \mathbb{R}^3$ and a uniquely defined normal $\hat{n}(\mathbf{r})$, where $\mathbf{r} \in \Omega$. It is assumed that the rest of space is homogeneous, and that the object is at rest. Consider a velocity field incident on this scatterer denoted by $\mathbf{v}^i(\mathbf{r})$. This generates a scattered velocity field given by $\mathbf{v}^s(\mathbf{r})$ and we define the total velocity field as $\mathbf{v}^t(\mathbf{r}) = \mathbf{v}^i(\mathbf{r}) + \mathbf{v}^s(\mathbf{r})$. These fields can be represented by equivalent potentials such that $\mathbf{v}^\xi(\mathbf{r}) = \nabla\Phi^\xi(\mathbf{r})$, for $\xi \in \{t, s, i\}$. A unique solution in $\Phi^t(\mathbf{r})$ is guaranteed through the Burton-Miller formulation, written in terms of these potentials:[4]

$$\begin{aligned}
&\mathcal{L}_{BM}[\Phi,\Omega](\mathbf{r}) = V^i(\mathbf{r}),\\
&\mathcal{L}_{BM}[\Phi,\Omega](\mathbf{r}) \doteq (1-\alpha)\left(\frac{\Phi}{2} - \mathcal{D}[\Phi,\Omega](\mathbf{r})\right)\\
&\qquad\qquad - \alpha\beta\mathcal{N}[\Phi,\Omega](\mathbf{r}),\\
&V^i(\mathbf{r}) \doteq (1-\alpha)\Phi^i(\mathbf{r}) + \alpha\beta\hat{n}\cdot\nabla\Phi^i(\mathbf{r}),
\end{aligned} \tag{1}$$

where $0 \le \alpha \le 1$, the constant weighting factor, and β, the coupling factor, make the solution unique at all frequencies; the optimal choice of alpha and beta has been the subject of many studies.[24–26] In the remainder of the paper we follow the standard Burton-Miller formulation.[4] Note, setting $\alpha = 0$ or $\alpha = 1$ introduces a non-trivial null space at frequencies

https://doi.org/10.1121/10.0001182

that correspond to the interior resonance of the structure. The reader is referred to Refs. 4, 27 for a theoretical explanation. Insight into the null spaces of these operators for spherical objects can be obtained using methods presented in Ref. 28. The operators $\mathcal{D}$ and $\mathcal{N}$ are defined as

$$\mathcal{D}[\Phi,\Omega](\mathbf{r}) \doteq \int_{\Omega} \Phi(\mathbf{r}')\hat{\mathbf{n}}(\mathbf{r}') \cdot \nabla' G(\mathbf{r},\mathbf{r}')d\mathbf{r}', \tag{2a}$$

$$\mathcal{N}[\Phi,\Omega](\mathbf{r}) \doteq \hat{\mathbf{n}}(\mathbf{r}) \cdot \nabla \left[\int_{\Omega} \Phi(\mathbf{r}')\hat{\mathbf{n}}(\mathbf{r}') \cdot \nabla' G(\mathbf{r},\mathbf{r}')d\mathbf{r}'\right]. \tag{2b}$$

We define the kernel as the free-space Helmholtz kernel, $G(\mathbf{r},\mathbf{r}') = e^{-ik_0|\mathbf{r}-\mathbf{r}'|}/4\pi|\mathbf{r}-\mathbf{r}'|$, k_0 is the wavenumber, $\beta = i/k_0$. An $e^{i\omega t}$ dependence is assumed and suppressed. The solution to these equations is typically effected in a discrete setting as follows; one discretizes Ω using a collection of patches such that $\Omega = \cup_l^{N_p}\Omega_l$, where Ω_l denotes a patch. Then each patch Ω_l supports a unique, locally indexed, set of basis functions $\psi_n(\mathbf{r})$, $n \in \{1,\ldots,N_v\}$. In other words, each basis function, ψ_n, is defined over a unique collection of patches $\Gamma_n = \{\Omega_\alpha,\ldots,\Omega_l,\ldots,\Omega_\beta\}$.

We can now state that $\Phi(\mathbf{r}) = \sum_{n=1}^{N_v} a_n\psi_n(\mathbf{r})$, where $\mathbf{r} \in \Gamma_l$; we provide a deeper analysis in the following sections. Using Gakerin testing, one arrives at a system of equations $\mathcal{Z}\mathcal{I} = \mathcal{V}$, where

$$\begin{aligned}
\mathcal{Z}_{mn} &= \langle \psi_m(\mathbf{r}), \mathcal{L}_{BM}[\psi_n,\Gamma_n](\mathbf{r})\rangle,\\
\mathcal{V} &= [v_1, v_2, \ldots, v_{N_b}]^T,\\
\mathcal{I} &= [a_1, a_2, \ldots, a_{N_b}]^T,
\end{aligned} \tag{3}$$

where $v_m = \langle \psi_m(\mathbf{r}), \mathcal{V}^i(\mathbf{r})\rangle = \int_{\Gamma_m} \psi_m(\mathbf{r})\mathcal{V}^i(\mathbf{r})d\mathbf{r}$.

Evaluating the hypersingular operator $\mathcal{N}$ that arises from the Galerkin Burton-Miller formulation [Eq. (3)], is ordinarily problematic, but even more so when we consider the difficulty of parameterizing and integration on higher order surfaces.[29–31] The usual remedy for these issues is to employ a special numerical integration scheme, which we will expound on later. Additionally, as shown below, this places strict limitations on the implementation of MLFMA when patch sizes grow to be large relative to a wavelength.

B. Description of geometry

Next, we provide a succinct overview of using subdivision surfaces for a closed surface triangular mesh in order to detail the shape description; we shall note that this section is provided purely for completeness and omits details that can be found in several references.[12,13,32] In particular, the flavor of subdivision that we use is based on Loop's seminal work.[12]

Consider an underlying triangular net of control points defined as a set of vertices and a connectivity map that will form an initial primal control mesh denoted by $\mathcal{T}_0$ at level 0. Next, we define the 0-ring of a patch (triangle) as the vertices that belong to the patch, and the 1-ring as the set of all vertices that can be reached by traversing no more than two edges, as shown in Fig. 1. We define the regularity of the triangle by the characterization of its vertices' valence (0-ring); the valence of a given vertex is the number of edges incident on itself. A vertex is considered regular if its valence is equal to 6, otherwise, it is called an irregular or extraordinary vertex. A triangle is regular if its vertices are all regular, and irregular otherwise.

A smooth limit surface can be generated by recursive refinements of original mesh's control points T_0. Given $\mathcal{T}_0$ where there are $\mathcal{K}_t$ triangles, the Loop subdivision scheme recursively subdivides a triangle of level k into four subtriangles of level $k+1$ by bisecting the edge of each triangle *and* adjusting their locations using a weighted information scheme, that is based on their neighboring vertices on the coarse mesh. It follows, that at each step we generate $4^k\mathcal{K}_t$ new triangular patches. After each subdivision, the position of every vertex will be recomputed and each new triangle patch can be reparameterized by a 1-ring of the patch; Fig. 1 shows a regular triangle, ϵ, defined by its 1-ring vertices indexed from 1 to 12.

Consider Fig. 1 again. Here, the true surface corresponding to a regular triangular patch ϵ, can be evaluated as $\mathbf{r}(u,v) = \sum_{i=1}^{N_v} \mathbf{c}_i\psi_i(u,v)$, where (u,v) are local barycentric coordinates, $\psi_i(\mathbf{r})$ is a box-spline basis function, $\mathbf{c}_i$ are vertex locations of the $N_v = 12$ control points. When a triangle has irregular vertices, the patch must be refined until the considered point lies in a regular patch such that we can reapply the method described above.[13] Accordingly, we redefine ψ_i as a subdivision basis set, and N_v as the total number of control nodes defined on the 1-ring of the triangular patch.

It has been shown that the basis functions $\psi_i(\mathbf{r})$ has the following properties: (a) they have compact support, (b) they are non negative, (c) they preserve convexity, and (d) they are C^2 continuous across regular patch boundaries and C^1 at irregular vertices.

C. Isogeometric basis sets and discrete systems

In Sec. II B, we have defined effective basis functions that act upon control vertices so as to produce a limit

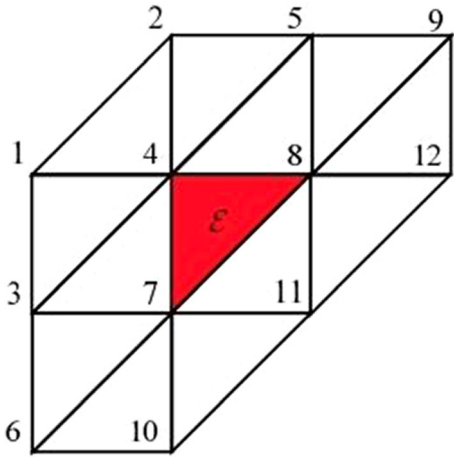

FIG. 1. (Color online) Regular triangular patch defined by its 1-ring vertices.

surface. In what follows, we *postulate* that one can define quantities at these control nodes that represent the physics on the limit surface. To this end, one can write the potential over any given patch as

$$\Phi(\mathbf{r}(u,v)) = \sum_{i=1}^{N_v} a_i \psi_i(\mathbf{r}(u,v)), \tag{4}$$

where now we define a_i as weights assigned to the locally indexed ith vertex; N_v, $\psi_i(\mathbf{r}(u,v))$, and (u, v) retain the same definition as those prescribed above. Employing Galerkin testing with these prescribed basis sets, one obtains

$$\mathcal{Z}\mathcal{I} = \mathcal{V}, \tag{5a}$$

$$Z_{mn} = \int_{\Gamma_m} \psi_m(\mathbf{r}) \mathcal{L}_{BM}[\psi_n, \Gamma_n](\mathbf{r}) d\mathbf{r}, \tag{5b}$$

where $\mathcal{I} = [a_1, a_2, \ldots, a_N]^T$, $\mathcal{V} = [V_1, V_2, \ldots, V_N]^T$, and

$$V_m = \int_{\Gamma_m} \psi_m(\mathbf{r}) V^i(\mathbf{r}). \tag{5c}$$

While simply stated, evaluation of these integrals is challenging from mulitple perspectives: the hypersingular nature of these integrals needs to be carefully taken into account when the support $\Gamma_m \cap \Gamma_n \notin \emptyset$. Likewise, higher order quadrature poses significant bottlenecks. These issues are addressed in Sec. III.

III. EVALUATION OF INNER PRODUCTS

As alluded to earlier, the principal challenge is the evaluation of matrix element Z_{mn}. The order of the basis function (for both geometry and physics) is fourth order. Naively, the order of the integration rule for evaluating the inner products scale as $N_q \propto 16$ per triangle, giving an effective scaling as $N_q^2 \propto 256 N_\Delta^2$, where N_Δ is the number of patches associated with the control vertices m and n; note that using N_Δ is an abuse of notation, as N_Δ can differ for ψ_m and ψ_n. As is apparent, this cost quickly dominates the overall cost. Note that if the two nodes are in proximity to each other, one needs additional structure to evaluate the hypersingular integrals, this interaction is illustrated in Fig. 2. The approach we espouse is to construct an adaptive quadrature scheme

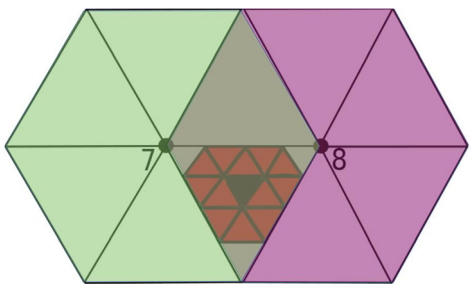

FIG. 2. (Color online) Interaction between two nodes wherein the black subpatch denotes the source, red patches are its nearfield neighbors, and all other patches lie in its farfield region.

that can be accelerated via wideband MLFMA. To set the stage for the computation, assume that each triangle in the domain Γ_n of the nth basis function is partitioned recursively into 4^l subpatches where $l \in \mathbb{N}$. The domain of each of these partitions is now denoted by Γ_n^γ for $\gamma = 1, \ldots, 4^l N_\Delta$. It follows that any matrix element can be computed in terms of its partial contributions such that

$$\begin{aligned} Z_{mn} &= \sum_\zeta \sum_\gamma \int_{\Gamma_m^\zeta} \psi_m(\mathbf{r}) \mathcal{L}_{BM}^\gamma \left[\psi_n(\mathbf{r}), \Gamma_n^\gamma\right] dS \\ &= \sum_\gamma \sum_\gamma Z_{mn}^{\zeta\gamma}, \end{aligned} \tag{6}$$

where $\mathcal{L}_{BM}^\gamma$ denotes the evaluation of the operator over the domain Γ_m^γ, and the summations are over the number of source and observation subpatches. In our implementation we have fixed the depth of recursion l. We note the following.

- The size of each sub-patch is typically sub-wavelength; often less than a tenth of a wavelength.
- If the interaction is a self interaction, i.e., $m = n$, and $\Gamma_m^\zeta = \Gamma_n^\gamma$, one needs to use Hadamard finite part integration.[2]

Next, we prescribe a methodology to ameliorate the cost of evaluating Eq. (6).

A. Amelioration of matrix vector product costs

To reduce the cost above, we take recourse to a tree based algorithm that is robust at small length scales. Fast multipole methods have long been in vogue in both acoustics and electromagnetics,[33] their use has been to reduce the cost of evaluating a matrix vector product. As has been shown in Chew *et al.*[34] the manner which this approach has been used is to first enclose the entire object in a cubical domain (henceforth, called the root node), and recursively subdivide until one reaches a prescribed size of the smallest box (henceforth, termed the leaf node). Then at each level one partitions interactions between all boxes at that level as being in each other's near or far field via the following rules: (a) any two boxes are in each other's near field provided they share a geometrical region in space (node/edge/face), (b) boxes are denoted as far field pairs *if* they are in each other's far field and their parents are in each other's near field. This partition of interactions ensures that near field interactions are done at the leaf level, and all other interactions are accounted for using far field operators at different levels in the tree; Fig. 3 illustrates this computational infrastructure. In effect, using the above computational procedure one computes a matrix vector product by partitioning $\mathcal{Z} = \mathcal{Z}^{near} + \mathcal{Z}^{far}$. The matrix $\mathcal{Z}^{near}$ is explicitly computed and stored, and $\mathcal{Z}^{far}$ is never explicitly computed. The product $\mathcal{Z}^{far}\mathcal{I}$ is effected via five tree operations; charge to multipole (C2M), multipole to multipole (M2M), multipole to local (M2L), local to local (L2L), and local to observer (L2O). These denote operations mapping radiation of

https://doi.org/10.1121/10.0001182

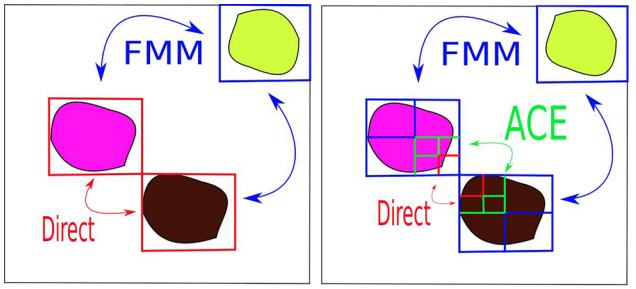

FIG. 3. (Color online) Comparison of interactions between FMM and wideband MLFMA. (a) Limit on traditional leaf box size means that interactions between large patches must be computed directly. (b) For wideband MLFMA, interactions between large patches may be split between nearfield and farfield such that favorable scaling is maintained.

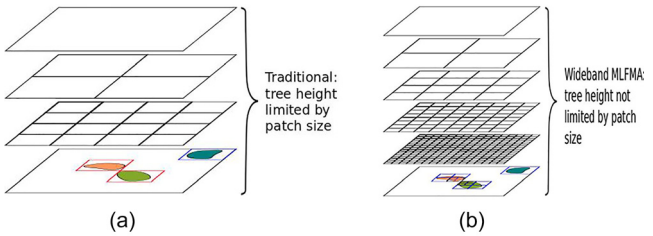

FIG. 4. (Color online) Illustration of traditional and wideband MLFMA trees. (a) Traditional: MLFMA leaf box size (and therefore tree height) is limited by the size of the largest patch. (b) Wideband MLFMA: leaf box size and tree height are not limited by patch size, and may be chosen for optimal MLFMA scaling.

sources onto a tree, traversal up and across the tree, and finally, mapping these fields onto observers. The nuances of these operations are discussed in several papers, but notationally consistent definitions can be found in Refs. 22, 23. Implicit in the above discussion is that one indirectly classifies interactions between basis functions.

The starting point of building a tree is to choose a leaf box size, typically chosen to be 0.2λ, where λ is the wavelength corresponding to the wavenumber k_0. All basis functions whose support, Γ_m, overlaps significantly with the domain of a leaf box are assigned to that box. In a typical discretization, the domain of each unknown is approximately 0.1λ. As a result, each unknown can be mapped into one leaf box. This is *not* the case for higher order discretizations wherein the domain of each basis function is significantly larger.[11] As a result, their domain would span multiple leaf boxes. One alternative is to make the leaf box size significantly larger, to say largest Γ_m, for $m = 1, \ldots, N_b$. An alternative would be to exploit the tree infrastructure to reduce the cost of computing each $Z_{mn} \in \mathcal{Z}^{near}$. It follows that given Eq. (6), the near interactions at the leaf node may instead be classified in terms of Γ_m^ζ and Γ_n^γ, and one can instead compute $Z_{mn}^{\zeta\gamma}$ and this collection constitutes $\mathcal{Z}^{near}$. But we can do better than previous work,[11] by choosing the leaf box size (and correspondingly, the size of Γ_m^ζ) to be arbitrarily small so as to achieve the optimal tradeoff between total computational cost for both near and far field computation; Fig. 3(b) illustrates these advantages. To enable choosing leaf box sizes smaller than 0.2λ, we use wideband FMM[22] that is stable at small lengths. With no loss in generality, we denote boxes whose side lengths are smaller than 0.2λ as accelerated Cartesian expansion[35](ACE) boxes, and those at that size or larger, as FMM boxes (see Fig. 4).

To this end, consider two leaf boxes that interact in the far field of each other. The domain of these leaf boxes are denoted using ω_s and ω_o, respectively. Assume that $\Gamma_n^\gamma \cap \omega_s \neq \emptyset$. Analogously, $\Gamma_m^\zeta \cap \omega_o \neq \emptyset$. Let $\mathbf{r}_o^c$ and $\mathbf{r}_s^c$ denote the centers of ω_o and ω_s. Then, using the notation introduced in Refs. 22, 35,

$$\int_{\Gamma_m^\zeta} \psi_m(\mathbf{r}) \mathcal{L}_{BM}^\gamma \left[\psi_n(\mathbf{r}), \Gamma_n^\gamma\right] = \mathcal{L}_A \circ \mathcal{T}_A \circ \mathcal{M}_A, \tag{7a}$$

where the operators are defined as

$$\mathcal{M}_A \doteq \left\{\mathbf{M}^{(0)}, \ldots, \mathbf{M}^{(P)}\right\},$$

$$\mathbf{M}^{(p)} = (-1)^p \int_{\Gamma_n^\gamma} d\mathbf{r}' \hat{n}' \cdot \nabla' \frac{(\mathbf{r}' - \mathbf{r}_s^c)^{(p)}}{p!} \psi_n(\mathbf{r}'), \tag{7b}$$

$$\mathcal{T}_A \circ \mathcal{M}_A \doteq \left\{\mathbf{L}^{(0)}, \ldots, \mathbf{L}^{(P)}\right\}$$

$$\mathbf{L}^{(p)} = \sum_{n=p}^{P} \nabla^{(n)} G(\mathbf{r}_o^c, \mathbf{r}_s^c) \cdot (n-p) \cdot \mathbf{M}^{(n-p)}, \tag{7c}$$

and

$$\mathcal{L}_A \circ \{\cdot\} = -\sum_{p=0}^{P} [(1-\alpha) + \alpha\beta\hat{n} \cdot \nabla](\mathbf{r} - \mathbf{r}_o^c)^{(p)} \cdot p \cdot \mathbf{L}^{(p)}. \tag{7d}$$

Equations (7b) and (7c) define C2M, M2L, and L2O operations. In the above expressions, $\mathbf{A}^{(n)}$ and $\mathbf{r}^{(n)}$ [whose component can be expressed in compressed form as $\mathbf{r}^{(n)}(n_1, n_2, n_3) = x^{n_1} y^{n_2} z^{n_3}$] denote an nth rank tensor and $\mathbf{C}^{(n-m)} = \mathbf{A}^{(n)} \cdot m \cdot \mathbf{B}^{(m)}$ denotes an m-fold contraction between tensors of rank n and m. It is apparent that Eq. (7c) depends only on centers of leafs boxes and *not* on either source or observation subtriangles. As a result, using Eq. (7c) for all source subtriangles in ω_s and observation subtriangles in ω_o enables cost savings. While these equations describe a 1-level setting, it can be extended to a multi-level wideband setting by nesting these operations;[22] note, details of these operators, proofs of convergence, cost complexity, etc., can be obtained from Refs. 22, 35.

B. Implementation details

In what follows, we lay out the algorithmic structure necessary to implement the formulation that has been outlined. Specifically, we will assume that one has an available geometric description comprising of control points, and a connectivity map regarding the neighborhood of each control point. In addition, we assume that one has the available

necessary tools to obtain limit quantities (surface/fields), their gradients, normals, and so on, given a barycentric coordinate. Given this initial set of tools, our algorithmic procedure is outlined in Fig. 5.

IV. COMPLEXITY ANALYSIS

In order to accurately analyze the complexity, we forgo studying our system with respect to the traditional measure N_b, total number of basis functions, and elect to cast the present scaling discussion in terms of the total number of unique quadrature points per patch.

We choose to do so, because N_b can obscure the true cost of setup and execution time, for a high order system, given the relatively large spatial extent of basis function support that can cause potential overlap. Furthermore, while asymptotic scaling is generally the metric of choice when discussing fast methods, one must be more careful when handling higher order methods as compared to lower order methods because the constants that appear in front of the asymptotic scalings are often significantly larger and can have a more pronounced impact on the relative cost of different formulations.

A. Computational complexity

Given the prior definitions, we make some assumptions that make asymptotic analysis tractable: these are (a) all basis functions are associated with the same number of patches ν, (b) the number of patches that share a nodal vertex is μ, (c) the average size of the patch used is approximately 0.2λ, and (d) the number of quadrature points used in any patch is N_q. The overall costs comprises three distinct portions; (a) costs to evaluate $\mathcal{Z}^{near}$, (b) cost to evaluate a matrix vector product with $\mathcal{Z}^{near}$, and (c) with $\mathcal{Z}_{far}$. Traditionally, the cost for filling $\mathcal{Z}$ costs $\mathcal{O}(N_b^2 N_q^2 \nu^2)$ The cost of a matrix vector product with $\mathcal{Z}$ is $\mathcal{O}(N_b^2)$.

To analyze costs associated the above scheme, let us start with traditional MLFMA. Assume that the leaf box size is 0.2λ, and one assigns patches (and *not* basis) to each leaf

Algorithm 1 A description of the overall algorithm

1: **Define:**

2: $\mathcal{T}_0$: control mesh

3: h: Average edge length per patch

4: Q: Order of high order integration rule

5: ℓ: level of refinement for integration scheme

6: $\Delta x_0 = h/2^\ell$: initialize leaf box size

7: **Initialize wideband MLFMA:**

8: initialize FMM, construct oct-tree

9: Assign $\approx Q/4^\ell$ integration points per subpatch

10: Assign centers of subpatches to leaf boxes

11: Construct near and far interaction list in terms of (sub) patches

12: **isoBEM:**

13: Compute and store partial sums in the nearfield using q.(6); $\mathcal{Z}^{Near} = \mathcal{Z}_{mn}$

14: Solve isoBEM system $\mathcal{Z}\mathcal{I} = \mathcal{V}$ using GMRES

15: Compute the matrix-vector product in GMRES using wideband MLFMA for remaining near-field contributions and far-field contributions

16: **Scattering Cross Section:**

17: Compute $\mathbf{f}(x)$, $\mathbf{f} : \Omega \to \mathbb{R}^3$, where $x \in \Omega$ {Map surface pressure onto farfield}

FIG. 5. Algorithm 1: A description of the overall algorithm.

https://doi.org/10.1121/10.0001182

box. This implies that there are $\mathcal{O}(1)$ patches per leaf box or, equivalently, $\approx N_p$ leaf boxes. This manner of constructing the tree implicitly assumes that some of the interaction between basis functions whose domain overlap, like that shown in Fig. 2, are constructed via MLFMA whereas other portions are constructed via direct integration. From these arguments, it follows that the cost of constructing $\mathcal{Z}^{near}$ scales as $\mathcal{O}(N_p N_q^2)$. The cost for each of the MLFMA steps scales as follows: $\mathcal{O}(N_p N_q)$ for C2M and L2O operations, and $\mathcal{O}(N_p \log N_p)$ for the rest of the tree operations. It is evident that both computing the near field as well as mapping on to the leaf level in a traditional MLFMA tree are the bottlenecks.

The story is slightly different for wideband MLFMA. For simplicity assume that each patch is divided into N_q subpatches, and the size of each leaf box is such that one has $\mathcal{O}(1)$ *subpatches*. This implies that there are approximately $N_p N_q$ leaf boxes. The cost of evaluating $\mathcal{Z}^{near}$ scales as $\mathcal{O}(N_p N_q)$. The cost of C2M and L2O scales as $\mathcal{O}(N_p N_q)$ and traversal up and down the tree as approximately $\mathcal{O}(N_p N_q \log(N_p N_q))$. As is apparent, the key difference between the two methods is a factor of N_q in the cost for near field. This is significant as N_q needs to be high enough to integrate a higher order function.

V. RESULTS

In this section, we present a number of results validating our isoBEM with respect to accuracy, efficiency, and computational complexity. Furthermore, we present solutions to scattering from conical and non-conical scatters and make the appropriate comparisons against analytic solutions and flatBEM; note, flatBEM is used to denoted a solution methodology that uses piecewise flat tesselations to represent the geometry, and constant basis functions to represent the potentials. For all examples in the proceeding, we note that the incident field propagates along $\hat{\mathbf{k}} = -\hat{\mathbf{z}}$ direction. The scattering cross (SCS) section[36] is used to as a metric to compare simulations, unless it is specified otherwise. All the cases demonstrated below assume that the test objects are sound-hard and are immersed in a homogeneous medium. The speed of sound in the ambient medium is assumed to be 343 m/s, and the dimensions of all objects analyzed in this paper are normalized with respect to the wavelength of the incident field. Finally, when errors are reported, they are the L_2 norm between computed and reference quantities.

A. Accuracy of wideband MLFMA for nearfield computations

As the rationale for using wideband MLFMA is to alleviate the computational complexity associated with nearfield computations, in what follows we examine the accuracy and efficacy of the proposed approach. The numerical experiments to evaluate the accuracy are conducted on a uniformly discretized sphere. As is done in traditional MLFMA, we first choose the largest size of the leaf box to be greater than the support of any basis function. Next, we choose the height of the tree such that all basis functions that share a supporting patch interact in the nearfield of each other. To fix the integration rule necessary to evaluate inner products, we choose the number of subdivisions per-patch and use low-order quadrature on each sub-patch. Specifically, we assume that each patch is sub-divided into 16 sub-patches. The resulting matrix or matrix-vector product (with any random vector) forms the benchmark for our subsequent tests. Next, we increase the height of the tree. Now, we would have contributions to the matrix vector product from both near and "far" interactions via ACE/MLFMA. Note, as ACE is low-frequency stable, it may be tempting to arbitrarily choose a very small leaf box. The optimal size of the leaf box is approximately the size of the largest sub-patch. Note, division of each patch is tantamount to defining a quadrature rule for each patch. This said, there are obvious tradeoffs. A very small leaf box implies that most of the computation is done in the farfield, i.e., numerically. This is inadvisable for hypersingular integrals as regularization within the FMM algorithm is not possible. Our scheme relies on the order of polynomials we need to evaluate over the surface (geometry and basis order), defining a quadrature rule, using a division of patches to achieve that rule, and then defining a leaf box size such that that number of near interactions are approximately $\mathcal{O}(1)$. On the finest division of a patch, we use a 3-point rule.

In our experiment, we choose a sphere of radius 2.63λ and a tree with leaf box of size $\Delta x_0 = 0.4\lambda$; we note that each patch consists of 16 subpatches. We truncate the tree at the leaf level, level $\mathcal{L}$ and compute all nearfield interactions. Next, we choose the leaf box at $\Delta x_0 = 0.2\lambda$, which translates to roughly 4 subpatches per leaf box. We then compute all the nearfield interactions and one level of MLFMA farfield. Again, we adjust the leaf box size to $\Delta x_0 = 0.1\lambda$, which allows 1 subpatch per leaf box and introduces two levels of MLFMA farfield. As all the tree computations using ACE, the number of terms in the expansion, P controls the accuracy. Figure 6 demonstrates the computational speedup and Fig. 7 describes the controllable accuracy as a

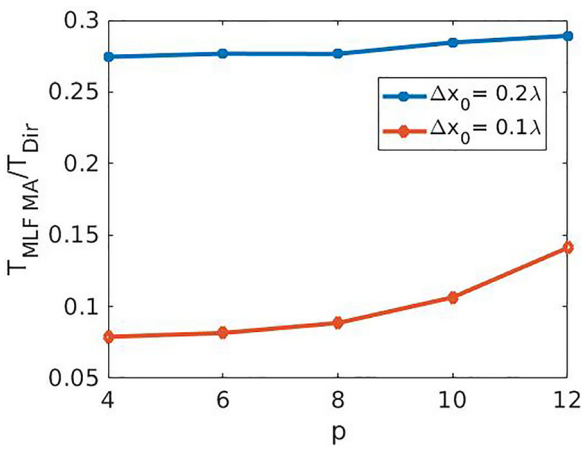

FIG. 6. (Color online) Comparison of isoBEM nearfield timings against the $\mathcal{O}(N_p^2 N_b^2 N_q^2)$ direct fill algorithm on a 2.63λ sphere, where P is the expansion coefficient.

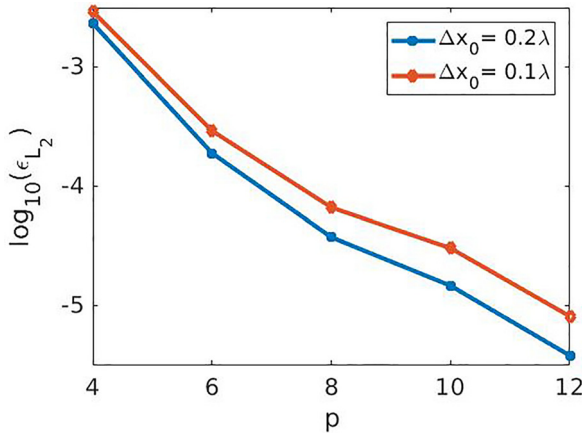

FIG. 7. (Color online) Convergence in relative L_2 error of matrix using isoBEM versus the $\mathcal{O}(N_p^2 N_b^2 N_q^2)$ direct fill algorithm on a 2.63λ sphere, where P is the expansion coefficient.

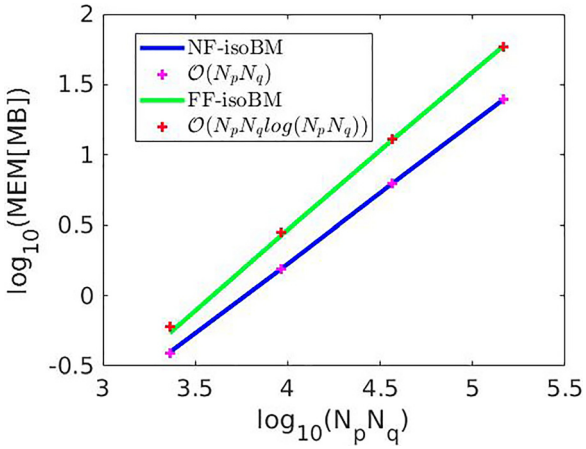

FIG. 9. (Color online) Scaling in nearfield and farfield memory for a series of boxes of size $1.151\lambda - 9.212\lambda$.

function of P. As is evident from these figures, one can control the accuracy and the corresponding speedup.

B. Computational complexity and storage of MFLMA BIE-subdivision

This section verifies the theoretical scaling for both complexity and storage, Figs. 8 and 9, in terms of total number of number of quadrature points per patch or N_pN_q; both experiments are conducted on a series of boxes of size $1.151\lambda - 9.212\lambda$.

In Fig. 8, we demonstrate the scaling of the timing of a single matrix-vector product. The scaling is $\mathcal{O}(N_pN_q \log(N_pN_q))$, as expected. In our careful analysis, we find that it is evident that the scaling is primarily from the farfield contributions and in particular dominated by the M2M and L2L stages; this results is as expected due to our system being higher order, thus demanding a high level integration rule.

Scaling in storage for the near and far fields are shown in Fig. 9. As expected, the nearfield memory scales linearly with respect to N_pN_q. The farfield memory, for our given experiment, is mostly dominated by the precomputation of the aggregation/disaggregation and translation operator and as a result we find scaling to be $\mathcal{O}(N_pN_q \log(N_pN_q))$.

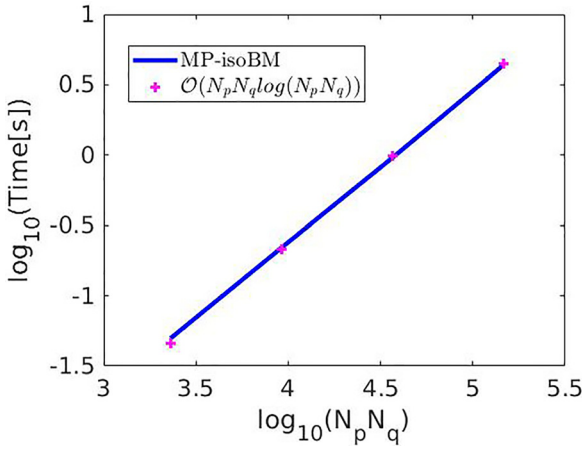

FIG. 8. (Color online) Scaling of MLFMA matrix vector product timings for a series of boxes of size $1.151\lambda - 9.212\lambda$.

C. Accuracy of isogeometric analysis

To validate and demonstrate the accuracy of the proposed approach, we consider scattering from a sphere discretized at multiple resolutions. To this end, we consider a sphere with radius of 1.0 m that is modeled using an initial control mesh comprised of 642 vertices and 1280 faces. Starting from this control mesh and performing two levels of Loop subdivision results in two meshes; the coarser mesh with 2562 vertices and 5120 faces, and finer mesh having 10 242 vertices and 20 480 faces, respectively. All three meshes have the *same* limit surface. This implies that an increase in the number of control points is equivalent to h-refinement as the support of the basis function changes and therefore, the approximation of the continuous operator $\mathcal{L}_{BM}\{\cdot\}$. The number of degrees of freedom (DoF) in isoBEM is equivalent to the number of vertices; consequently, the three tests have 642, 2562, and 10 242 DOFs, respectively. By comparing those obtained using isoBEM with analytic series approach, the relative L_2 errors in surface pressure are 0.0591, 0.0180, and 0.00750, respectively, for these three different discretizations. As is evident, the accuracy in the potential in the L_2 norm is excellent and it is convergent.

Finally, Fig. 10 makes a direct comparison between farfield data obtained using isoBEM, on the sphere of one level of refinement corresponding to 5120 unknowns, and flatBEM on the sphere of two level of refinement corresponding to 20 480 unknowns, and analytical solutions. We find there to be excellent agreement between all three data sets.

D. Analysis of non-conical geometries

Next, to demonstrate the viability of using isoBEM we compare results obtained using this method against those obtained using flatBEM. In all cases analyzed here, the

https://doi.org/10.1121/10.0001182

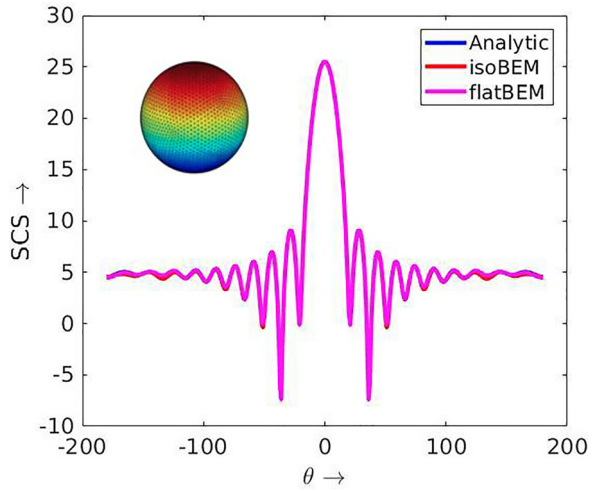

FIG. 10. (Color online) Scattering cross section of the sphere ($\phi = 0$ cut).

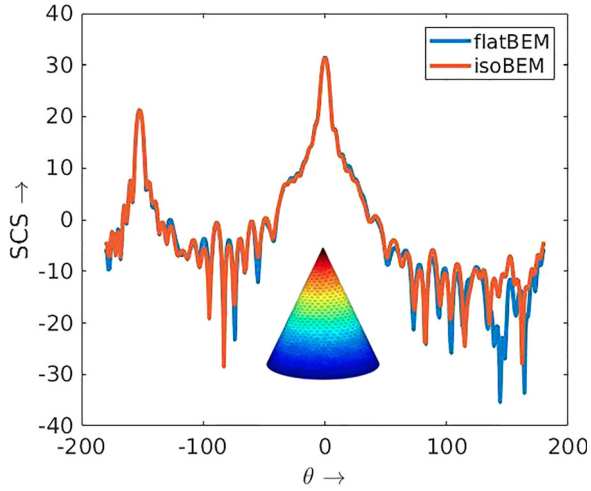

FIG. 12. (Color online) Scattering cross section of a 5.71λ by 11.66λ by 5.71λ cone ($\phi = 0$ cut).

discretization of objects used for analysis via flatBEM is such that its surface area is approximately identical to that used for isoBEM (within 99%). Note, to achieve this agreement, one needs a higher number of flat tesselations to mimic the higher order nature of subdivision surfaces. Finally, we also remind the reader that the number of degrees of freedom for flatBEM corresponds to the triangles whereas those for isoBEM corresponds to vertices (more precisely, control points).

We start with analyzing scatter from a torus that fits within a box of size 8.1λ by 8.1λ by 2.3λ. The number of degrees of freedom for flatBEM is 61 312 whereas those for isoBEM is 7664. As is evident from Fig. 11 the agreement between the two is excellent.

Next, we consider a cone that fits in a 5.71λ by 11.66λ by 5.71λ bounding box. Again, flatBEM uses 59 424 degrees of freedom while the isoBEM has 7430 degrees of freedom; Fig. 12 demonstrates the agreement between the two.

Finally, we consider a warhead that fits in a 4.57λ by 13.80λ by 4.57λ bounding box. The flatBEM uses 85 504 degrees of freedom whereas that using isoBEM uses 10 690. As in all the previous cases, the two sets of data is shown in Fig. 13 where we see that they agree very well with each other.

VI. SUMMARY

In this paper, our principal contribution is the development of an isogeometric anlaysis tool for scattering from rigid bodies using the Burton-Miller formulation. The basis sets we have chosen arise from subdivision representation of the geometry; the benefits of this representation are that the resulting representation are C^2 almost everywhere. Unfortunately, this high degree of regularity implies that high order functions are used for representing both the geometry and physics. This translates to high numerical quadrature that can overwhelm overall costs. Indeed, this has been a *persistent* challenge for all higher order methods. Our secondary contribution in this paper is an extension of the wideband multi-level fast multipole method to efficiently evaluate both components of the matrices and inner products with them. Through numerous numerical results, we have shown the efficacy of this approach in terms of accuracy against analytical data, comparison against

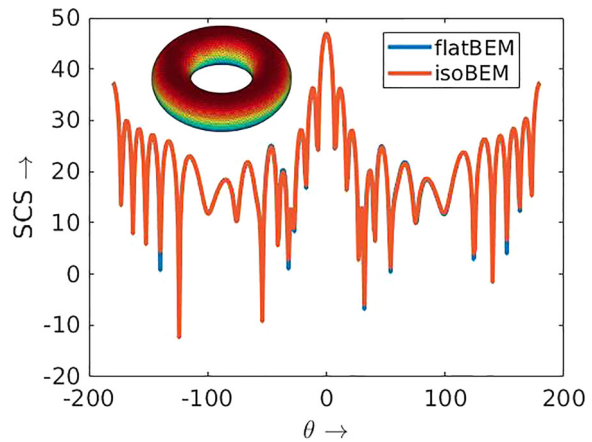

FIG. 11. (Color online) Scattering cross section of a 8.1λ by 8.1λ by 2.3λ torus ($\phi = 0$ cut).

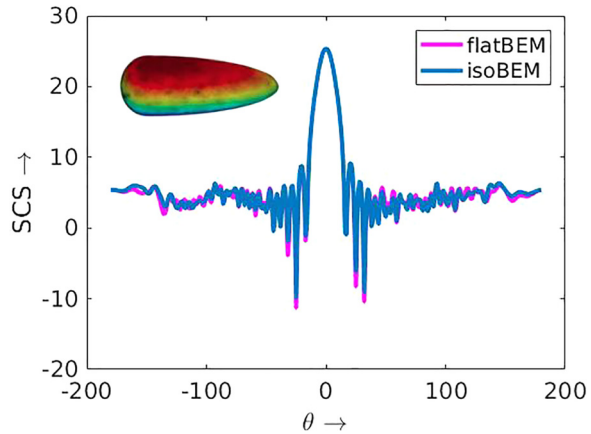

FIG. 13. (Color online) Scattering cross section of a 4.57λ by 13.80λ by 4.57λ warhead ($\phi = 0$ cut).

piecewise flat triangulation for non-conical objects, and cost complexity for acoustically large objects. Overall, isogeometric analysis tools with the necessary mathematical augmentation permit efficient analysis directly from a CAD representation. Our future research is on using this framework for design optimization and will be presented elsewhere.

ACKNOWLEDGMENT

The authors acknowledge computing support from the HPC Center at Michigan State University and financial support from NSF via Grant No. CMMI-1725278.

APPENDIX

This appendix is provided to ensure this paper is self-contained such that the reader can build upon this work. In order to implement subdivision, we refer the reader to Refs. 37–39 for open source code and the corresponding documentation. Our method builds upon this framework. Furthermore, details on the isogeometric boundary element method and its implementation can be found in Refs. 39 and 40.

[1]S. Kirkup, *The Boundary Element Method in Acoustics* (Integrated Sound Software, Todmorden, UK, 2007), Vol. 8.
[2]T. Terai, "On calculation of sound fields around three dimensional objects by integral equation methods," J. Sound Vib. **69**, 71–100 (1980).
[3]R. E. Kleinman and G. F. Roach, "Boundary integral equations for the three-dimensional Helmholtz equation," SIAM Rev. **16**, 214–236 (1974).
[4]A. J. Burton and G. F. Miller, "The application of integral equation methods to the numerical solution of some exterior boundary-value problems," Proc. R. Soc. London A **323**, 201–210 (1971).
[5]S. Amini and P. J. Harris, "A comparison between various boundary integral formulations of the exterior acoustic problem," Soc. Ind. Appl. Math. **84**, 59–75 (1990).
[6]L. Gaul, M. Fischer, and U. Gauger, "Accuracy and efficiency of the multipole Galerkin BEM for acoustics," Theor. Comput. Acoust. **2003**, 97–106 (2004).
[7]M. Fischer, U. Gauger, and L. Gaul, "A multipole Galerkin boundary element method for acoustics," Eng. Anal. Bound. Elem. **28**, 155–162 (2004).
[8]N. A. Gumerov and R. Duraiswami, "A broadband fast multipole accelerated boundary element method for the 3D Helmholtz equation," J. Acoust. Soc. Am. **125**, 191–205 (2009).
[9]A. Peterson, "Mapped vector basis functions for electromagnetic integral equations," Synth. Lect. Comput. Electromagn. **1**(1), 1–124 (2006).
[10]N. V. Nair, B. Shanker, and L. Kempel, "Generalized method of moments: A boundary integral framework for adaptive analysis of acoustic scattering," J. Acoust. Soc. Am. **132**, 1261–1270 (2012).
[11]D. Dault and B. Shanker, "A mixed potential MLFMA for higher order moment methods with application to the generalized method of moments," IEEE Trans. Ant. Propag. **64**(2), 650–662 (2016).
[12]C. Loop, "Smooth subdivision surfaces based on triangles," Master's thesis, Department of Mathematics, University of Utah, Salt Lake City, UT (1987).
[13]J. Stam, "Evaluation of Loop subdivision surfaces," in *SIGGRAPH'98 CDROM Proceedings*, Citeseer (1998).
[14]T. J. R. Hughes, J. A. Cottrell, and Y. Bazilevs, "Isogeometric analysis: CAD, finite elements, NURBS, exact geometry and mesh refinement," Comput. Meth. Appl. Math. **194**(39-41), 4135–4195 (2005).
[15]J. A. Cottrell, A. Reali, Y. Bazilevs, and T. J. R. Hughes, "Isogeometric analysis of structural vibrations," Comput. Meth. Appl. Math. **195**, 5257–5296 (2006).
[16]B. Hassani, S. M. Tavakkoli, and N. Z. Moghadam, "Application of isogeometric analysis in structural shape optimization," Sci. Iran. **18**, 846–852 (2011).
[17]J. Li, D. Dault, B. Liu, Y. Tong, and B. Shanker, "Subdivision based isogeometric analysis technique for electric field integral equations for simply connected structures," J. Comput. Phys. **319**, 145–162 (2016).
[18]J. Li, X. Fu, and B. Shanker, "Formulation and iso-geometric analysis of scalar integral equations for electromagnetic scattering," IEEE Trans. Ant. Propag. **66**, 1957–1966 (2018).
[19]J. Li, D. Dault, and B. Shanker, *New Trends in Computational Electromagnetics* (Institute of Engineering and Technology, London, 2020), Chap. New trends in geometric modeling and discretization of integral equations, pp. 315–372.
[20]X. Fu, J. Li, and B. Shanker, "Generalized Debye sources-based EFIE solver on subdivision surfaces," IEEE Trans. Ant. Propag. **65**, 5376–5386 (2017).
[21]R. N. Simpson, M. A. Scott, M. Taus, D. C. Thomas, and H. Liane, "Acoustic isogeometric boundary element analysis," Comput. Meth. Appl. Math. **269**, 265–290 (2014).
[22]V. Melapudi, H. Huang, B. Shanker, and T. Van, "A novel wideband FMM for fast integral equation solution of multiscale problems in electromagnetics," IEEE Trans. Ant. Propag. **57**(7), 2094–2104 (2009).
[23]S. Hughey, H. M. Aktulga, V. Melapudi, L. Mingyu, B. Shanker, and E. Michielssen, "Parallel wideband MLFMA for analysis of electrically large, nonuniform, multiscale structures," IEEE Trans. Ant. Propag. **67**(2), 1094–1107 (2019).
[24]S. Amini, "On the choice of the coupling parameter in boundary integral formulations of the exterior acoustic problem," Appl. Anal. **35**(1-4), 75–92 (1990).
[25]S. Marburg, "The Burton and Miller method: Unlocking another mystery of its coupling parameter," J. Comput. Acoust. **24**, 1550016 (2015).
[26]C. J. Zheng, H. Chen, H. F. Gao, and L. Du, "Is the Burton–Miller formulation really free of fictitious eigenfrequencies?," Eng. Anal. Boundary Elem. **59**, 43–51 (2015).
[27]T. C. Lin, "A proof for the Burton and Miller integral equation approach for the Helmholtz equation," J. Math. Anal. Appl. **103**, 565–574 (1984).
[28]J. Li, D. Dault, and B. Shanker, "A quasianalytical time domain solution for scattering from a homogeneous sphere," J. Acoust. Soc. Am. **135**(4), 1676–1685 (2014).
[29]M. Guiggiani and A. Gigante, "A general algorithm for multidimensional Cauchy principal value integrals in the boundary element method," J. Appl. Mech. **57**, 906–915 (1990).
[30]M. Guiggiani, G. Krishnasamy, T. J. Rudolphi, and F. J. Rizzo, "A general algorithm for the numerical solution of hypersingular boundary integral equations," J. Appl. Mech. **59**, 604–614 (1992).
[31]D. S. Weile and X. Wang, "Strong singularity reduction for curved patches for the integral equations of electromagnetics," IEEE Ant. Wire. Propag. Lett. **8**, 1370–1373 (2009).
[32]F. Cirak, M. Ortiz, and P. Schröder, "Subdivision surfaces: A new paradigm for thin-shell finite-element analysis," Int. J. Numer. Methods Eng. **47**, 2039–2072 (2000).
[33]R. Coifman, V. Rokhlin, and S. Wandzura, "The fast multipole method for the wave equation: A pedestrian prescription," IEEE Trans. Antennas Propag. **35**, 7–12 (1993).
[34]W. C. Chew, J. M. Jin, E. Michielssen, and J. Song, *Fast and Efficient Algorithms in Computational Electromagnetics* (Artech House, Boston, 2000).
[35]B. Shanker and H. Huang, "Accelerated cartesian expansions—A fast method for computing of potentials of the form $R^{-\nu}$ for all real ν," J. Comput. Phys. **226**(1), 732–753 (2007).
[36]D. L. Colton and R. Kress, *Integral Equation Methods in Scattering Theory* (Wiley, New York, 1983).
[37]PiXar, "Opensubdiv," http://graphics.pixar.com/opensubdiv/docs/intro.html (Last viewed 04/28/2020).
[38]F. de Goes, M. Desbrun, M. Meyer, and T. DeRose, "Subdivision exterior calculus for geometry processing supplemental material: Subdivision rules," ACM Trans. Graph **35**, 133 (2016).
[39]J. Li, "Integral equations in computational electromagnetics: Formulations, properties and isogeometric analysis," Ph.D. thesis, Michigan State University, Lansing, MI (2018).
[40]J. Dolz, H. Harbrechta, S. Kurz, M. Multerer, S. Schops, and F. Wolf, "The fast isogeometric boundary element C++ library for Laplace, Helmholtz, and electric wave equation," arXiv:1906.00785 (2019).